

Multiphase cooperation for multilevel strain accommodation in a single-crystalline $BiFeO_3$ thin film

Wooseon Choi, Bumsu Park, Jaejin Hwang, Gyeongtak Han, Sang-Hyeok Yang, Hyeon Jun Lee, Sung Su Lee, Ji Young Jo, Albina Y.Borisevich, Hu Young Jeong, Sang Ho Oh, Jaekwang Lee, and Young-Min Kim

Citation: Chin. Phys. B, 2024, 33 (**9**): 096805. DOI: 10.1088/1674-1056/ad62e0
Journal homepage: http://cpb.iphy.ac.cn; http://iopscience.iop.org/cpb

What follows is a list of articles you may be interested in

Symmetry quantification and segmentation in STEM imaging through Zernike moments

Jiadong Dan, Cheng Zhang, Xiaoxu Zhao(赵晓续), and N. Duane Loh
Chin. Phys. B, 2024, 33 (**8**): 086803. DOI: 10.1088/1674-1056/ad51f4

Anomalous strain effect in heteroepitaxial $SrRuO_3$ films on (111) $SrTiO_3$ substrates

Zhenzhen Wang(王珍珍), Weiheng Qi(戚炜恒), Jiachang Bi(毕佳畅), Xinyan Li(李欣岩), Yu Chen(陈雨), Fang Yang(杨芳), Yanwei Cao(曹彦伟), Lin Gu(谷林), Qinghua Zhang(张庆华), Huanhua Wang(王焕华), Jiandi Zhang(张坚地), Jiandong Guo(郭建东), and Xiaoran Liu(刘笑然)
Chin. Phys. B, 2022, 31 (**12**): 126801. DOI: 10.1088/1674-1056/ac8725

Fabrication of $GaAs/SiO_2/Si$ and GaAs/Si heterointerfaces by surface-activated chemical bonding at room temperature

Rui Huang(黄瑞), Tian Lan(兰天), Chong Li(李冲), Jing Li(李景), and Zhiyong Wang(王智勇)
Chin. Phys. B, 2021, 30 (**7**): 076802. DOI: 10.1088/1674-1056/abf917

Electro-optical dual modulation on resistive switching behavior in $BaTiO_3/BiFeO_3/TiO_2$ heterojunction

Jia-Jia Zhao(赵佳佳), Jin-Shuai Zhang(张金帅), Feng Zhang(张锋), Wei Wang(王威), Hai-Rong He(何海蓉), Wang-Yang Cai(蔡汪洋), Jin Wang(王进)
Chin. Phys. B, 2019, 28 (**12**): 126801. DOI: 10.1088/1674-1056/ab54b4

Structural and physical properties of $BiFeO_3$ thin films epitaxially grown on $SrTiO_3$ (001) and polar (111) surfaces

He Shu-Min (贺树敏), Liu Guo-Lei (刘国磊), Zhu Da-Peng (朱大鹏), Kang Shi-Shou (康仕寿), Chen Yan-Xue (陈延学), Yan Shi-Shen (颜世申), Mei Liang-Mo (梅良模)
Chin. Phys. B, 2014, 23 (**3**): 036801. DOI: 10.1088/1674-1056/23/3/036801

SPECIAL TOPIC — Stephen J. Pennycook: A research life in atomic-resolution STEM and EELS

Multiphase cooperation for multilevel strain accommodation in a single-crystalline $BiFeO_3$ thin film

Wooseon Choi[1,†], Bumsu Park[2,†], Jaejin Hwang[3,†], Gyeongtak Han[4], Sang-Hyeok Yang[1], Hyeon Jun Lee[5], Sung Su Lee[6], Ji Young Jo[6], Albina Y. Borisevich[7], Hu Young Jeong[8], Sang Ho Oh[9,‡], Jaekwang Lee[3,§], and Young-Min Kim[1,¶]

[1] *Department of Energy Science, Sungkyunkwan University (SKKU), Suwon* 16419, *Republic of Korea*
[2] *Samsung Electronics, Hwaseong* 18448, *Republic of Korea*
[3] *Department of Physics, Pusan National University, Busan* 46241, *Republic of Korea*
[4] *LG Energy Solution, Daejeon* 34122, *Republic of Korea*
[5] *Department of Materials Science and Engineering, Kangwon National University, Republic of Korea*
[6] *School of Materials Science and Engineering, Gwangju Institute of Science and Technology (GIST), Gwangju 61005, Republic of Korea*
[7] *Center for Nanophase Materials Sciences, Oak Ridge National Laboratory, TN* 37831, *USA*
[8] *Graduate School of Semiconductor Materials and Devices Engineering, Ulsan National Institute of Science and Technology (UNIST), Ulsan* 44919, *Republic of Korea*
[9] *Department of Energy Engineering, KENTECH Institute for Energy Materials and Devices, Korea Institute of Energy Technology (KENTECH), Naju* 58330, *Republic of Korea*

(Received 22 April 2024; revised manuscript received 10 July 2024; accepted manuscript online 15 July 2024)

The functionalities and diverse metastable phases of multiferroic $BiFeO_3$ (BFO) thin films depend on the misfit strain. Although mixed phase-induced strain relaxation in multiphase BFO thin films is well known, it is unclear whether a single-crystalline BFO thin film can accommodate misfit strain without the involvement of its polymorphs. Thus, understanding the strain relaxation behavior is key to elucidating the lattice strain–property relationship. In this study, a correlative strain analysis based on dark-field inline electron holography (DIH) and quantitative scanning transmission electron microscopy (STEM) was performed to reveal the structural mechanism for strain accommodation of a single-crystalline BFO thin film. The nanoscale DIH strain analysis results indicated a random combination of multiple strain states that acted as a primary strain relief, forming irregularly strained nanodomains. The STEM-based bond length measurement of the corresponding strained nanodomains revealed a unique strain accommodation behavior achieved by a statistical combination of multiple modes of distorted structures on the unit-cell scale. The globally integrated strain for each nanodomain was estimated to be close to -1.5%, irrespective of the nanoscale strain states, which was consistent with the fully strained BFO film on the $SrTiO_3$ substrate. Density functional theory calculations suggested that strain accommodation by the combination of metastable phases was energetically favored compared to single-phase-mediated relaxation. This discovery allows a comprehensive understanding of strain accommodation behavior in ferroelectric oxide films, such as BFO, with various low-symmetry polymorphs.

Keywords: $BiFeO_3$, scanning transmission electron microscopy, electron holography, multiferroic material, strain mapping

PACS: 68.37.Ma, 61.05.jp, 77.55.Nv, 68.55.–a **DOI:** 10.1088/1674-1056/ad62e0

1. Introduction

As a paradigmatic research platform, strain engineering[1,2] has been extensively conducted to modify the physical properties of perovskite epitaxial thin films, such as ferroelectricity,[3] flexoelectricity[4–6] and their coupled orders with magnetism.[7,8] Particularly, emergent functionalities of multiferroic $BiFeO_3$ (BFO) thin films have garnered considerable attention over the last two decades because they are highly sensitive to a slight change in lattice strain imposed by substrate templates.[9] When the BFO film grows without structural misfit defects and chemical alteration, their resulting functionalities are primarily attributed to a strain-induced phase change because BFO possesses an intricate set of structural polymorphs that are closely related in energy.[10–12] As the structural variants are closely coupled with polar cation displacements or oxygen octahedral tilts/rotations, complex strain relaxation behavior may be expected.[9] Nanoscale phase separation, as a typical characteristic of the strain accommodation behavior of BFO films at a high strain level of $\sim 2\%$, was observed through macroscopic analyses, such as x-ray reciprocal space mapping and piezoresponse force microscopy.[13–15] Atomic-level observation through scanning transmission electron microscopy (STEM) has verified that

[†] W. Choi, B. Park, and J. Hwang contributed equally to this work.
[‡] Corresponding author. E-mail: shoh@kentech.ac.kr
[§] Corresponding author. E-mail: jaekwangl@pusan.ac.kr
[¶] Corresponding author. E-mail: youngmk@skku.edu

© 2024 Chinese Physical Society and IOP Publishing Ltd

the strain-induced nanophases are adjacent to each other with abrupt morphotropic phase boundaries,[14,16] demonstrating the formation of a multiphase BFO thin film.

At a moderate level of misfit strain, such as when a BFO film is grown on a $SrTiO_3$ (STO) substrate (which imparts a compressive strain of approximately -1.5%), a single-phase BFO film can be obtained, and the phase evolves from tetragonal (T) to monoclinic (M) to distorted rhombohedral (R) as the strain relaxes with increasing film thickness.[17–20] A phenomenological interface that distinguishes a strained bottom layer from a relaxed top layer is known to be created at a critical thickness ($\sim$ 15 nm for BFO/STO) and acts as a boundary that determines the structural phase and ferroelectric functionalities.[21,22] The film grown above the critical thickness (t_c) begins to relax its accumulated strain through a structural phase transition, with the intervention of structural defects, or through a complex interplay between oxygen octahedral tilts (OOTs) or rotations and polar distortions. The artificially imposed strain can be inhomogeneously distributed within the interior of the film during strain relaxation, generating a strain gradient. Owing to electromechanical coupling, the strain gradient induces a built-in electric field that alters ferroelectric polarization, which is known as flexoelectricity.[23] The strain gradient is typically assumed to be vertical toward the direction of film growth, in which strain relaxation occurs progressively. However, in addition to the clamping effect of the step edges on the substrate, in-plane components of strain gradient can be generated, which can alter the self-polarization direction of the BFO film.[6] The x-ray peak broadening of the BFO (00l) reflection observed in experimental results is considered to be a signature of the inhomogeneous strain originating from the relaxed part of the film,[21,24] which indicates that different regions of the film may differ in relaxation behaviors with OOTs and ferroelectric variants.[25] However, it remains unclear whether the misfit strain is relieved in a single-phase BFO film through the combination of various possible structural degrees of freedom, owing to the absence of precise atomic-scale information, which may be a key parameter to understand the subdued flexoelectric effect in the as-grown single-phase form.

In this study, we report multilevel-strained structures combined with multiple phases to effectively accommodate the misfit strain in a single-crystalline epitaxial BFO thin film. Through correlative strain analysis combined with nanoscale dark-field inline electron holography (DIH) and atomic-scale bond length measurement based on STEM, we reveal the hierarchical structure of different strain states and phases in an epitaxial BFO film grown on a $SrRuO_3$ (SRO)/STO substrate under compressive strain (approximately -1.5%). Density functional theory (DFT) calculations help understand the advantage of multilevel strain accommodation assisted by multiple phases over single-phase-mediated strain relaxation. Our results, correlatively obtained at multiple length scales, provide a comprehensive understanding of strain accommodation in thin-film materials with multiple structural degrees of freedom, such as in BFO.

2. Results and discussion

2.1. Heteroepitaxial $BiFeO_3$ film and interface structure

A 55 nm-thick BFO film was epitaxially grown on top of a 37 nm-thick SRO film on STO (001). In this study, we adopted the SRO epitaxial buffer layer because it helps to maintain the lattice coherency up to larger thicknesses.[25,26] Previous studies[21,27] have demonstrated that the grown BFO film has a single-crystalline monoclinic structure (Cc) with an $a^-b^-c^-$ OOT pattern, and the polar order differs below and above t_c because of lattice–charge coupling.

To explore the overall film structure and interface at atomic resolution, we performed high-angle annular dark-field (HAADF)-STEM, as shown in Figs. 1(a)–1(c). A low-magnification HAADF-STEM image shows the heterostructure of BFO/SRO/STO combined with the formation of sharp interfaces (Fig. 1(a)). No lattice misfit defects or secondary phases at the interface between the BFO film and SRO/STO substrate are observed in a larger field of view (Fig. S1), which is consistent with the previous XRD results.[21] We further characterized the interfacial structures of the triple heterostructure using atomic-resolution HAADF-STEM. Figures 1(b) and 1(c) show the interface structures of BFO/SRO and SRO/STO, respectively, verifying that all three lattices are perfectly matched along the in-plane direction without the intervention of misfit defects. This finding suggests that the BFO film may be fully strained on the SRO/STO substrate. Previous experiments have revealed that BFO can tolerate a wide range of strain from compressive (-2.6%) to tensile ($+1.2\%$) and transform its crystalline phase from tetragonal to orthorhombic over the strain range.[28–30] Considering the in-plane lattice mismatch between the BFO film ($a = 3.965$ Å) and STO ($a = 3.905$ Å) substrate, the BFO film is subjected to a compressive strain of approximately -1.5% at which the monoclinic phase (M_A) is stabilized.[31] However, phase stability also depends on film thickness. At a thickness of 60 nm–70 nm, rhombohedral-like BFO can grow without structural relaxation,[8,29,32] which may be attributed to the collective modification of OOTs for the accommodation of strain.[15] The simulated HAADF-STEM images with the atomic models of the two heterointerfaces corroborate that BFO grows on the SRO/STO substrate with a defect-free and abrupt interface. The critical thickness of the BFO film strained to the STO substrate, in which the polarization is suppressed owing to the competitive lattice–charge coupling effect, was experimentally measured to be $\sim$ 15 nm by mapping the polar

displacements of the Fe ions (Fig. S2), which is consistent with the t_c value of the previous study.[21] At a larger thickness above t_c, it has been generally perceived that inhomogeneous strain gradient often occurs as a function of the distance from the interface, resulting in strain relaxation.[24,33,34] The strain gradient can induce a large internal electric field on the order of 1 MV/m–10 MV/m attributed to electromechanical coupling, namely, flexoelectricity, which is large enough to change the physical properties of the films.[36,37] The accumulated strain is presumed to be released continuously as the film grows thicker, unless misfit dislocations or defects are introduced to relax it. However, there has been no direct demonstration of single-crystalline BFO films to verify the relaxation or accommodation of misfit strain inside the film at a fundamental level.

To gain insights into the strain relief of single-crystalline BFO films at the unit-cell level, we measured the local lattice distortions for different regions denoted by A (close to the surface) and B (contiguous to the interface) in Fig. 1(a) via local bond length mapping.[6,11] This well-established method numerically determines the projected atom positions of every lattice composed of four Bi atoms, resulting in the generation of a map exhibiting a local bond length change for all the assigned lattices with a pico-scale precision.[36,37] The measurement precision of the bond length is demonstrated to achieve a level of ± 2 pm by minimizing the beam-scanning artifact (Fig. S3). Figures 1(d) and 1(e) show the pixelated maps representing the c/a ratio obtained by dividing the lattice distortion map in the out-of-plane (c-axis) direction by that in the in-plane (a-axis) direction. The false color-coded contrast in each pixel of the map indicates the relative ratio of the measured lattice parameters for the two orthogonal axes. Therefore, the c/a ratio maps spatially describe the process of straining individual lattices in two regions that exhibit different c/a ratios. The average c/a ratios of regions A and B are 1.00 ± 0.04 and 1.04 ± 0.03, respectively. This result suggests that the strain state of the BFO lattice differs at different locations inside the film. The average lattices deduced from the mapping results are schematically shown in Fig. 1(f). Tetragonal-like distortions are notable in region B, whereas the lattices in region A tend to exhibit cubic-like structures. When considering gradual strain relief, these results may agree with those of previous studies;[6,38] tetragonal distortion is favored in the BFO lattice under compressive strain below the critical thickness. However, given that the in-plane (a-axis) lattice spacings are the same in both regions, these results are unlikely to represent the inhomogeneous strain distribution (strain gradient) of the entire film, but rather imply that the strain relaxation behavior is more complex. The relative strain field mapping at a larger nanoscale by geometric phase analysis, which can map local displacement fields by comparing relative phase shifts of a particular set of noncolinear Fourier components,[39–41] supports such complicated strain distribution (Fig. S4). The observed uneven strain distribution might not solely originate from the consequence of strain relaxation in itself, because atomic defects and local non-stoichiometry in the film significantly affect the resulting lattice structure and physical properties. To determine whether there is a probable effect of chemical variations, such as cation off-stoichiometry and oxygen vacancies, on the lattice distortion, we performed STEM–energy-dispersive x-ray spectroscopy (EDX) and STEM–electron energy loss spectroscopy (EELS) for the BFO film (Fig. S5); the corresponding results did not show any evidence of off-stoichiometry in the BFO film. Therefore, the issue of chemical variation can be neglected.

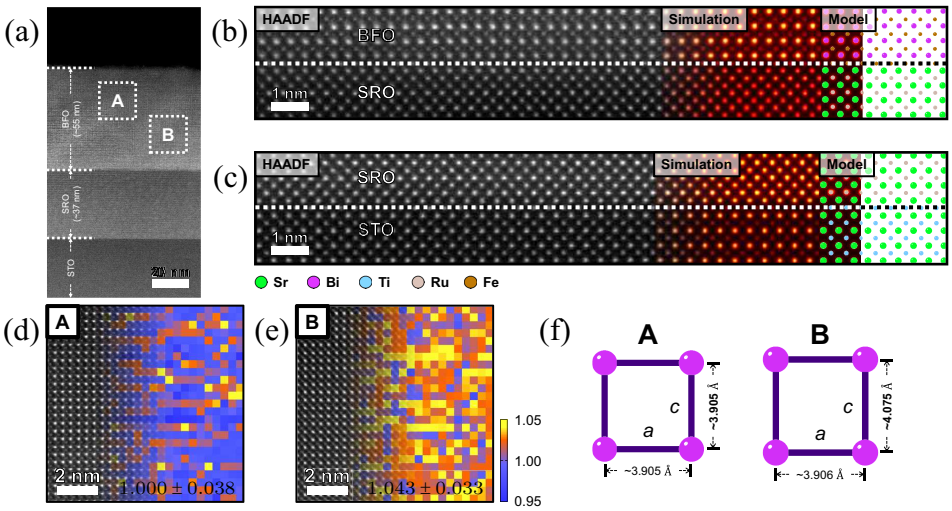


Fig. 1. Thin-film structure and local lattice distortions. (a) High-angle annular dark-field scanning electron transmission microscopy (HAADF-STEM) image of a [100] pseudo-cubic-oriented $BiFeO_3$ (BFO) thin film grown on a 37 nm-thick $SrRuO_3$ (SRO) buffer layer/$SrTiO_3$ (STO) substrate. (b) and (c) Magnified HAADF-STEM images of atomic structures of BFO/SRO and SRO/STO interfaces. Simulated HAADF-STEM images and corresponding interface models are shown on the right. (d) and (e) Lattice distortion maps showing c/a ratios for the two different regions marked A and B in panel (a). (f) Schematic models derived from the c/a values of the A and B regions.

2.2. Multilevel structures for strain accommodation in a single-crystalline BFO film

To analyze the nanoscale strain distribution in the BFO film, we adopted DIH[42] for in-plane strain mapping by selecting the $(010)_{pc}$ reflection (Fig. 2(a)). For comparison, the DIH-based in-plane strain map is shown alongside the corresponding region imaged through HAADF-STEM. Intriguingly, we observed that the in-plane lattice strain develops to multimodal states across the entire BFO film, resulting in the formation of strain nanodomains, while that of the SRO buffer layer exhibits no distinct strain fluctuation — fully strained to the STO substrate. Evidently, the in-plane strain is inhomogeneously distributed but does not show any correlation with the film thickness. This behavior is substantially different from that observed in conventional epitaxial films. Strikingly, despite this characteristic strain undulation, the net in-plane strain integrated over the entire area of the DIH strain map is almost zero, signifying that the film fully accommodates the misfit strain imposed by the SRO/STO substrate. Figure 2(b) shows the unusual strain fluctuation of the BFO film from a bird's eye view. Although the entire film is globally subjected to a compressive strain of approximately -1.5%, three types of domains with different strain states are distinguished at the nanoscale: compressive (C), tensile (T), and strained (S) to the SRO/STO substrate. The amplitude range of the in-plane strain is approximately $\pm 2.0\%$, and the gradual conversion of the strain mode from C to S then to T or vice versa occurs within ~ 20 nm. This strain range is considered far beyond the value ($< 1\%$) at which bulk materials begin to crack.[24,43]

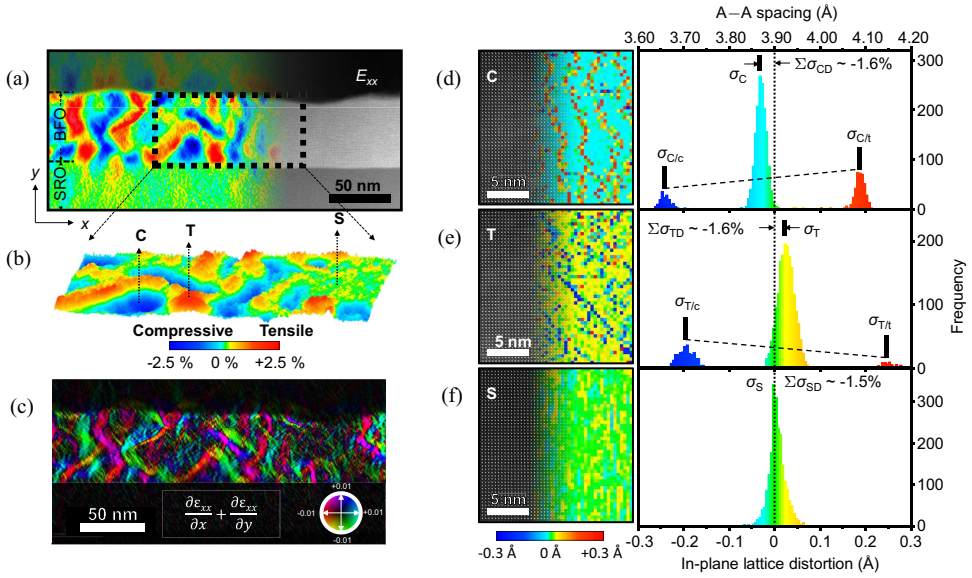


Fig. 2. Multilevel strain distribution inside the BFO thin film. (a) In-plane strain map obtained by dark-field inline holography, overlaid on an ADF STEM image of the film structure. (b) Perspective view of the BFO region with the strain undulation marked by a rectangle in panel (a). Three different strain modes, compressive (C), tensile (T), and strained (S) to the bulk STO substrate, and the undulation amplitude of the strain was measured to be approximately $\pm 2.0\%$. (c) Perspective visualization of the strain gradient map calculated from the experimental strain map, (b) differentiation (uphill gradient: cyan, downhill gradient: red). Strain gradient map was processed by applying an edge-preserving smoothing filter with an average of nine pixels in the dark-field inline electron holography strain map, which was implemented using the ImageJ software package. (d)–(f) In-plane lattice distortion maps of three distinctive strained phases (C, T, and S) marked in panel (b). Note that the in-plane lattice parameter corresponding to bulk STO ($a = 3.905$ Å, substrate) is used as a reference for all the strain maps. Scale bars are 5 nm.

In a ferroelectric epitaxial film above its critical thickness, it is presumed that the internal strain begins to relax across a region of several tens of nanometers with a decreasing slope in the out-of-plane direction, which then induces a built-in electric field inside the film owing to electromechanical coupling. This phenomenon is referred to as flexoelectricity.[6,23,24] The flexoelectricity-driven electric field has been regarded as an attribute of spontaneous polarization states characterized using the following relation: $E_f \approx \left(\frac{e}{4\pi\varepsilon_0 a}\right)\frac{\partial u_{ij}}{\partial z_k}$, where E_f is the generated electric field, e is the electronic charge, ε_0 is the permittivity of free space, a is the lattice constant, u_{ij} is the elastic strain, and z_k is the position coordinate related to the direction of the strain gradient.[24] As the built-in electric field is proportional to the strain gradient, the conversion of different strain states between strain domains at the nanoscale results in large strain gradient. Given that a strain of 2% changes within ~ 20 nm across strain nanodomains on average (Fig. 2(c)), the strain gradient is approximately 1.25×10^6 m^{-1}, which is similar to the value measured in oxide epitaxial films using grazing incidence in-plane x-ray diffraction.[35] Owing to the limitation of projective observation of the structure using transmission electron microscopy (TEM), it is unlikely to quantitatively estimate the three-dimensional strain tensors. However, the in-plane lattice strain is irregularly distributed over the film, exhibiting a ridge-and-valley pattern, and varies sharply between small regions less than 20 nm–

30 nm in width with no preferred orientation. This intricate strain landscape concomitantly gives rise to a locally undulated strain gradient, as visualized by the differentiation of the DIH strain map in Fig. 2(c). This large but localized strain gradient may induce a built-in electric field greater than 5 MV/m across the strain domain boundary under the flexoelectric effect. This roughly estimated value seems reasonable compared to the experimentally obtained strain gradient for the BFO film ($\sim$ 8.7 MV/m) by the Williamson–Hall plot.[6] In addition, it is considered to be large enough to influence the local physical properties of the BFO film. In ferroelectric materials, thermodynamically equivalent polar states are spontaneously formed in small regions with different orientations, referred to as the ferroelectric domains.[44] Domain configurations (size and orientation) are affected by various factors such as domain wall energy, electric field, and elastic energy. Lee *et al.*[35] revealed that a flexoelectricity-driven electric field above 1 MV/m leads to the formation of self-poled domains in as-grown ferroelectric films. Considering the localized strain gradient without a specific orientation preference observed in the BFO film (Fig. 2(c)), it is presumed that the ferroelectric domain structure is affected by the intricate distribution of strain-gradient-induced electric fields, resulting in the formation of nanodomains inside the BFO film. The ferroelectric nanodomain structure is considered as a structural feature in single-crystalline BFO films grown on STO substrate using atomic-resolution STEM.[12]

The measured range of the strain amplitude ($\pm$2.0%) from DIH indicates that the in-plane lattice spacing should vary in the range of $\pm$8 pm from that of STO (3.905 Å), which is measurable through our STEM-based bond length analysis with a small measurement error of $\pm$2 pm (Fig. S3). To assess the in-plane lattice spacings for the three representative strain states, C, T, and S, we acquired atomic-scale HAADF-STEM images of the three regions corresponding to each strain state and mapped the two-dimensional distribution of the in-plane lattice spacings for each unit cell. Images on the left in Figs. 2(d)–2(f) show that the three regions with different strain states exhibit varying levels of in-plane lattice spacings. Considering the color scale, the maps for the C and T regions predominantly exhibit cyan and yellow colors, respectively, whereas the S region exhibits a greenish-pixelated map. These results provide a unit-cell-level evidence for the presence of three characteristic strain states (C, T, and S states) in the single-crystalline BFO film: the regions with different in-plane spacings (on average) strikingly show a one-to-one correspondence with the regions with different nanoscale strain states revealed by DIH mapping (Figs. 2(b) and 2(d)–2(f)).

The analysis of the strain maps of the C and T regions shows that each unit-cell-wise map is not entirely homogeneous, but rather contained many outliers (exhibiting different color scales) far beyond the statistical noise level. To determine whether they are statistically significant, histograms were obtained for each strain map (graphs on the right in Figs. 2(d)–2(e)). Notably, two more strain states were involved as minor contributors to strain accommodation in both the strained C and T nanodomains at the unit-cell level, whereas the S region manifested a single strain mode that was fully strained to the STO lattice (a = 3.905 Å). These results revealed that seven different strain modes worked together for which the in-plane misfit strain in the BFO film was accommodated in a multifaceted manner, including three primary strain modes at the nanoscale and four subordinate strain modes at the unit-cell scale, which were hierarchically structured. The three primary strain modes were denoted as σ_{C}, σ_{T}, and σ_{S} for nanoscale strain distribution in the C, T, and S regions and the four secondary strain modes were denoted as $\sigma_{\mathrm{C/c}}$, $\sigma_{\mathrm{C/t}}$, $\sigma_{\mathrm{T/c}}$, and $\sigma_{\mathrm{T/t}}$ featured in the unit-cell-scale strain distribution of the C and T domains. The small characters of c and t indicated that new extreme compressive (c) and tensile (t) strain states of the unit cells appeared inside the nanoscale strain domains. The measured parameters for each strain mode are listed in Table 1.

Table 1. Measured parameters of seven different strain modes of BFO.

Level	Sym.	Average $d_{\text{in-plane}}$ (Å)	$d_{\text{in-plane}}$ relative to bulk STO (%)	In-plane strain vs. bulk BFO (%)	Occupancy (%)
Primary	σ_{C}	3.87	−0.77	−2.40	71
Secondary	$\sigma_{\mathrm{C/c}}$	3.66	−6.15	−7.69	8
Secondary	$\sigma_{\mathrm{C/t}}$	4.09	4.87	3.15	21
Primary	σ_{T}	3.93	0.77	−0.88	82
Secondary	$\sigma_{\mathrm{T/c}}$	3.70	−5.13	−6.68	15
Secondary	$\sigma_{\mathrm{T/t}}$	4.16	6.67	4.92	3
Primary	σ_{S}	3.90		−1.51	100

$\Sigma\sigma_{\mathrm{CD}} = (0.71 \times \sigma_{\mathrm{C}}) + (0.08 \times \sigma_{\mathrm{C/c}}) + (0.21 \times \sigma_{\mathrm{C/t}}) \simeq -1.6\%$,
$\Sigma\sigma_{\mathrm{TD}} = (0.82 \times \sigma_{\mathrm{T}}) + (0.15 \times \sigma_{\mathrm{T/c}}) + (0.03 \times \sigma_{\mathrm{T/t}}) \simeq -1.6\%$,
$\Sigma\sigma_{\mathrm{SD}} = \sigma_{\mathrm{S}} \simeq -1.5\%$.

For the domain fully strained to the STO substrate (S region, Fig. 2(f)), the typical unimodal distribution of the measured in-plane spacings corroborates the region being entirely strained by approximately −1.5% ($\Sigma\sigma_{\mathrm{SD}}$, where SD represents the strained domain to STO). The SRO buffer layer grown on the STO substrate remains fully strained to the STO substrate without local strain perturbation, as demonstrated in the DIH map (Fig. S6). In addition, the primary peak (σ_{C}) in the histogram of region C (Fig. 2(d)) shifts to a more compressive region by −0.77% in comparison with the peak in the S region (Fig. 2(f)), whereas the one (σ_{T}) in the T region (Fig. 2(e)) represents a relative peak shift toward the tensile region by 0.77%. The range of this apparent bipolar strain perturbation can translate into a fluctuating compressive strain ranging from −2.4% to −0.88% from the perspective of bulk BFO (Table 1). Eventually, the primary change in the strain state at

the nanoscale represents a perturbation in the magnitude of the compressive strain, not the true tensile strain.

In the unit-cell-wise secondary level of strain relaxation, we remarkably observed extreme states of compressive or tensile strain (far beyond $\pm 2.0\%$) that have been accessed only by theoretical frameworks.[25] A range of misfit strains from -2.5% to $+1.3\%$ has been experimentally applied to grow various BFO films by pulsed laser deposition.[9] In region C (Fig. 2(d)), two distinctive secondary strain states were detected: a compressive strain ($\sigma_{C/c}$) of -7.69% and tensile strain ($\sigma_{C/t}$) of 3.15%. Two similar extreme strain states also evolved in the T region: a compressive strain ($\sigma_{T/c}$) of -6.68% and tensile strain ($\sigma_{T/t}$) of 4.92%. These values seem to be systematically shifted by less than 2% toward the tensile strain compared to the C region, which is a similar magnitude to strain difference between σ_C and σ_T. Furthermore, the unit cells under extreme tensile strain prevailed over those under the counterpart compressive state in the C region. In contrast, the situation was reversed in the T region (comparing the peak heights of $\sigma_{C/c}$, $\sigma_{C/t}$, $\sigma_{T/c}$, and $\sigma_{T/t}$). Remarkably, the sums ($\Sigma\sigma_{CD}$ and $\Sigma\sigma_{TD}$) of all the strain states in each region were of the same value of approximately -1.6%, which was similar to the value ($\Sigma\sigma_{SD} = -1.5\%$) of the fully strained S region. This intriguing result suggested that the single-crystalline BFO film was globally subjected to a common compressive strain state imposed by the SRO/STO substrate, regardless of the local strain states of the nanodomains at both the nanoscale and unit-cell level. The apparent strain behavior of the BFO film appeared consistent, yet it exhibited distinct differences across specific nanoregions. This phenomenon may be ascribed to the coexistence of multiple structural variants of BFO that are energetically similar under a certain strain.[11,13,25] This aspect will be discussed later in the context of the strain-induced morphotropic phase changes based on the theoretical considerations.

2.3. Phase transition under strain gradient

The rhombohedral (R)-like BFO film exhibited a remarkable tolerance to a wide range of strains from compressive to tensile in an order of several percentages up to the thicknesses of 60 nm–70 nm, without causing structural defects. This result might be primarily attributed to the interplay of various intrinsic structural factors that can cooperate to accommodate epitaxial strain.[8,29,32] However, monoclinic (M) BFO was usually stabilized near or above the thickness of 15 nm below the thickness range, whereas a pure tetragonal phase of BFO was obtained in the ultrathin film regime (< 10 nm).[17,45] Considering the mesoscopic dependence on the film thickness, our BFO film (55 nm in thickness) comprised a mixture of R- and M-like BFO structures. Previous x-ray diffraction studies identified the dominant phase as monoclinic.[21] However, our recent findings revealed a more complex structural behavior. Microscopic observations via multimodal strain mapping revealed seven distorted lattices with different c/a ratios that emerged to accommodate the misfit strain and that they exhibited a hierarchical structure over multiple length scales. The coexistence of multiple phases at different strain states might be one of the primary contributors to the commonly observed x-ray diffraction peak broadening.

A change in the internal stress of the BFO film can induce a phase transition, accompanied by a change in the orientation of the ferroelectric polarization.[13] The path of this phase change depends on the level of the strain state, and the strain-induced R–M_A–M_C–T symmetry change was observed with increasing compressive strain. This strain-driven phase transition results in the evolution of the morphotropic phase boundary (MPB), which leads to the intimate coexistence of multiple phases due to strain relaxation.[14,30,46] In the vicinity of the MPB, the phase change occurred abruptly, accompanied by a change in physical properties. A recent study demonstrated that this abrupt phase change occurred across the MPB even in a doped BFO film at the unit-cell level.[47] However, such coexistence of multiple phases has not been observed in pristine single-crystalline BFO films. Considering the nanoscale strain behavior, the strain gradually changed between the domains. However, at the unit-cell level, the lattice structure varied abruptly within the interior C and T strain domains by a unit of the single unit cell. This result indicated that the MPB evolved inside the C and T strain domains at the unit-cell level as a pathway to accommodate internal strains, forming a multilevel-strained structure. In this respect, a question naturally arises as to how lattices are distorted when they reside across the strain domain boundary. As strain gradient occurs at the broad boundary, the lattices are likely to gradually morph their shapes from one phase to another, for example, following the pathway of phase change from tetragonal- to orthorhombic-like phases in reaction to the strain gradient manifested in several tens of nanometers.

To examine the unit-cell-wise structural distortion across the strain domain boundary, the same bond length analysis was performed for the boundary regions exhibiting the transitions from C-to-T nanodomains and vice versa. These regions were correlatively selected on the basis of the DIH strain map results. Figures 3(a) and 3(c) represent the HAADF-STEM images of the boundary regions and the corresponding in-plane lattice distortion maps. The uphill strain gradient is observed nearly along the horizontal direction (Fig. 3(a)). Conversely, the downhill strain gradient is noticeable in the opposite direction of growth (Fig. 3(c)). The averaged profiles of the lattice distortion maps (right graphs in Figs. 3(a) and 3(c)) show the uphill gradient from the compressive to tensile strain of the in-plane spacings and the downhill gradient with the opposite order of strain, respectively. Considering the change in the in-plane lattice spacings, the c/a ratio maps and the corresponding profiles exhibit a gradual change across the two boundary regions exhibiting the C-to-T transition (Fig. 3(b)) and the re-

verse transition from the T-to-C states (Fig. 3(d)). Given the progressive change in the c/a ratio through the boundary region, the phase change from the T- to O-like structure was observed to gradually occur through broad boundaries. However, considering the unit-cell-scale distortion, the unit cells were not collectively and systematically distorted to follow a directional strain gradient between two different strain states, but rather exhibited different values of distortion that were statistically distributed to accommodate strain inhomogeneity.

The multilevel characteristic of strain relief behavior observed in single-crystalline BFO films is summarized. Firstly, the three different strain states evolved in the entire BFO film on the nanoscale, forming strain nanodomains. Secondly, within a single strain nanodomain, multiple phases with unusual strain states that exhibit extremely tensile (up to 4.9%) or compressive (down to -7.7%) strain on the unit-cell level were identified to cooperatively participate in the overall strain compensation in the two different nanodomains (C and T regions) compared to the normal one (S region) that was fully strained to the STO substrate. Thirdly, the strain gradients developed across the broad boundaries, and the different levels of distorted unit cells were statistically distributed to accommodate a gradual change of strain state. Finally, the sum of all the unit-cell level strains, regardless of the strain states of nanodomains, pointed to a single value of negative strain ($\sim -1.5\%$), as globally expected for the growth on the STO substrate. This finding suggests that the multilevel involvement of different strain states or phases for overall strain accommodation in a single-crystalline BFO film may be energetically favored even at the unit-cell level, although this concept has been demonstrated in the case of BFO films with a nanoscale phase-mixture configuration. These unexpected results are anticipated to provide a new perspective for comprehensively understanding the strain accommodation mechanism in single-crystalline BFO films.

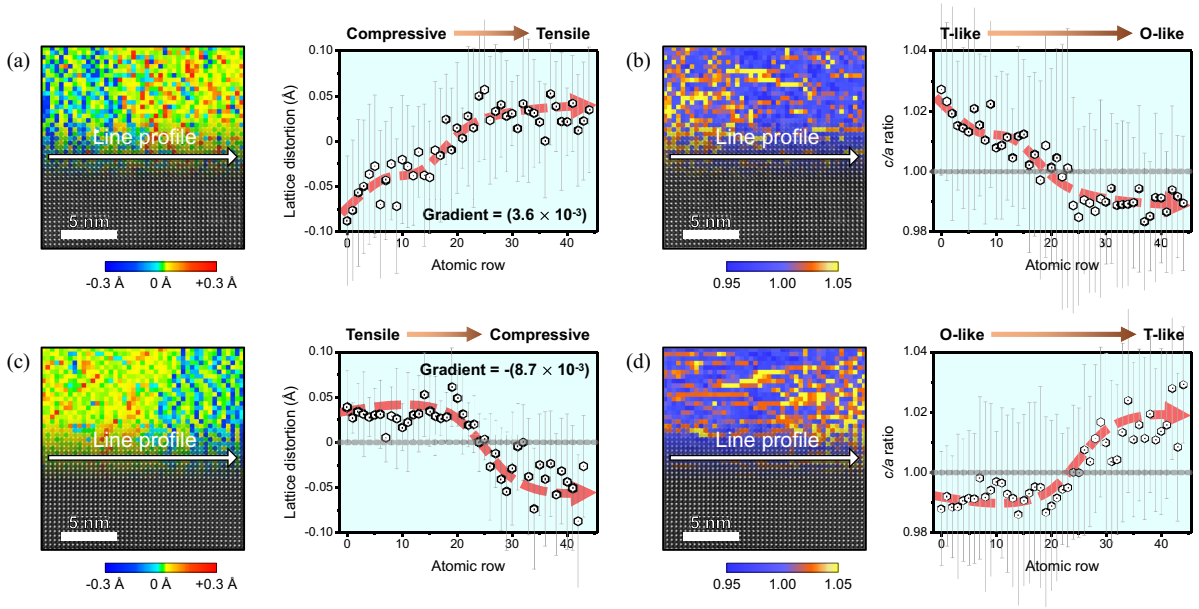


Fig. 3. Morphotropic O(MB)–R(MA)–T(MC) phase transitions across strain domains. (a) In-plane lattice distortion map and corresponding profile of the BFO region exhibiting phase transition from C-to-T nanodomains. (b) c/a ratio map and corresponding profile of the BFO region exhibiting phase transition from C-to-T nanodomains. (c) In-plane lattice distortion map and corresponding profile of the BFO region exhibiting phase transition from T-to-C nanodomains. (d) c/a ratio map and corresponding profile of the BFO region exhibiting phase transition from T-to-C nanodomains.

2.4. Energy relation between lattice strain and metastable phases

To elucidate the possibility of this multilevel coexistence of different phases for strain accommodation, we explored the evolution of the total energy for tetragonal (T), rhombohedral (R), and orthorhombic (O) BFO as a function of in-plane lattice distortion by performing the DFT calculations (see Fig. 4(a)). In-plane lattice distortion is defined as $(a-a_0)$, where a_0 is the theoretically optimized in-plane lattice constant for free cubic $SrTiO_3$, and a is the selected in-plane lattice constant for BFO. The misfit strain is defined as $(a-a_0)/a_0$ and is specified at the top x axis for reference. The calculated equilibrium lattice parameters of STO and BFO at the PBEsol GGA level were 3.908 Å and 3.946 Å, respectively. Therefore, BFO had less than approximately 1.0% compressive strain in the calculations, which was 0.5% smaller than that in the real experiment. Figure 4(a) shows that the total energy of T phase is minimized at approximately -0.15 Å distortion corresponding to approximately -4% misfit strain, whereas O phase is stabilized at approximately $+0.25$ Å distortion corresponding to approximately $+6\%$ misfit strain (Table 2). The energy of the R phase was always lower than that of the T and O phases at misfit strains ranging between -4% and $+6\%$. These results suggested that when the compressive strain exceeded -4%, the T phase became more energet-

ically favorable than the R phase, and a phase transition of BFO occurred from the R to T phase. In contrast, for tensile strains above 6%, the O phase was energetically more stable than the R phase, and likewise, BFO changed from the R to O phase. Interestingly, the total energies of the T and O phases were approximately 0.1 eV/f.u. higher than that of the R phase, which indicated that three different T, R, and O phases were very close in energy within 0.1 eV/f.u. Therefore, we considered the partition function of a BFO polymorph system whose three energy levels were composed of the minimum energy for each phase: $Z = \sum \exp(-\beta E)$, where Z is the partition function, $\beta = 1/(k_B T)$, k_B is Boltzmann's constant, T is the temperature and E is the minimum energy. Based on this partition function, the probability of existence of each phase with energy E is given by $P = -\exp(\beta E)/Z$. For the T and O phases, the probability P is estimated to be approximately 12% and 8.2%, respectively, at room temperature (Fig. 4(b)), which agrees with the experimental occupancy results of the BFO secondary phases (Table 1). Moreover, a BFO polymorph system indeed behaved like a physical system with a discrete set of energy eigenstates at the atomic scale. Moreover, single T or O phases did not exist independently because their misfit strains exceeded -4% and 6% (corresponding to -5% and $+5\%$ strain with respect to bulk BFO). However, to accommodate this large misfit strain, T and O phases prefer to coexist because the net misfit strain is reduced to less than 2%. Consequently, the secondary T and O phases ($\sigma_{C/c}$ with $\sigma_{C/t}$ and $\sigma_{T/c}$ with $\sigma_{T/t}$) were simultaneously observed in the experiment. In addition, we explored whether each of the two primary phases (σ_C and σ_T) coexisted with two secondary phases. In particular, the two extreme $\sigma_{C/c}$ and $\sigma_{T/t}$ phases were not probable because they were under huge strain even though their energies were only 0.1 eV/f.u. According to DFT calculations (Table 2), $\sigma_{C/c}$ is under -5.2% compressive strain and $\sigma_{T/t}$ is under 5.9% tensile strain for the bulk BFO. However, if two extreme $\sigma_{C/c}$ and $\sigma_{T/t}$ coexist with primary σ_C and σ_T with equal signs of strain, the applied strain to extreme $\sigma_{C/c}$ and $\sigma_{T/t}$ can be further accommodated by the amount of applied strain to the two primary phases. In the experiment, σ_C and σ_T exhibit equal signs of -0.77% and $+0.77\%$ misfit strains (Table 1), respectively. In the DFT calculations, σ_C and σ_T are selected as the phases with -0.51% and $+0.51\%$ misfit strain (Table 2), which is similar to the experimental values. Based on these values, all primary phases were estimated to be very close in energy within only a few meV/f.u. Therefore, two primary phases were introduced without energy cost to accommodate the large strain applied to the two extreme $\sigma_{C/c}$ and $\sigma_{T/t}$ phases.

Table 2. DFT-calculated strain value and energy of seven different strain modes of BFO.

Level		Sym.	Average $d_{\text{in-plane}}$ (Å)	$d_{\text{in-plane}}$ relative to bulk STO (%)	In-plane strain vs. bulk BFO (%)	Energy (meV/f.u.)	Occupancy (%)
T phase	secondary	$\sigma_{C/c}$ $\sigma_{T/c}$	3.76 ± 0.02	-3.84 ± 0.5	-4.7 ± 0.5	~ 0.11	$\sim 12\%$
	primary	σ_C	3.89	-0.51	-1.4		
R phase	primary	σ_S	3.91		-1.0	~ 0.0	$\sim 79.8\%$
	primary	σ_T	3.93	0.51	-0.4		
O phase	secondary	$\sigma_{C/t}$ $\sigma_{T/t}$	4.16 ± 0.02	6.39 ± 0.5	3.4 ± 0.5	~ 0.12	$\sim 8.2\%$

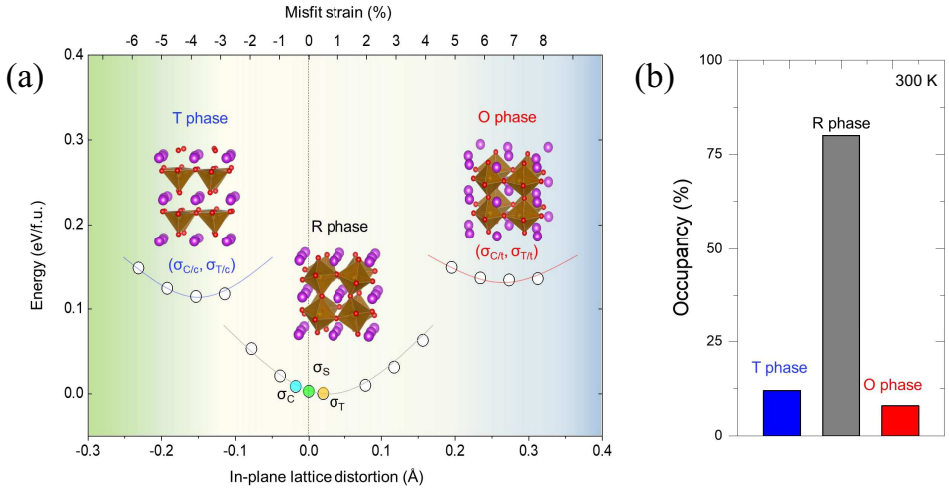


Fig. 4. DFT-calculated energy of the BFO polymorphs as a function of in-plane lattice distortion. (a) Evolution of the energy of BFO phases as a function of in-plane lattice distortion. The top x axis represents misfit strain. A negative value implies compressive strain, and a positive value implies tensile strain. The blue, black, and red lines represent parabolic fits to the data. Note that the DFT-optimized lattice parameter of bulk STO ($a = 3.908$ Å) is used as reference. (b) Probability of obtaining R- and O-like phases (occupancy) at room temperature, which is obtained using the partition function for three energy levels.

3. Experimental details

3.1. Film growth and x-ray diffraction analysis

Pulsed laser deposition (PLD) technique was utilized to grow $BiFeO_3$ films with a pseudo-cubic [001] growth direction at an oxygen partial pressure of 20 mTorr at 700 °C. A $SrRuO_3$ buffer layer with the thickness of $\sim$ 37 nm that was fully strained to a (001)-oriented $SrTiO_3$ substrate was prepared before the BFO growth, which helped to maintain strain coherency up to a larger thickness of the BFO film. A KrF excimer laser with a wavelength of 248 nm, an energy density of 1.5 J/cm^2, and a repetition rate of 2 Hz was used in the PLD. A high-resolution x-ray diffractometer (Advanced D8, Bruker) was used to survey the overall crystallographic phase of the grown BFO film and the rocking curve of the $(002)_{BFO}$ Bragg reflection as a function of the film thickness.

3.2. STEM-EDX/EELS analysis and simulations

Cross-sectional TEM samples of the BFO/SRO/STO heteroepitaxial films were prepared using a dual-beam focused ion beam system (FIB, Helios 450F1, Thermo Fisher Scientific) at an accelerating voltage of 15 kV. A low-voltage Ga-ion beam of 2 kV with a low incident angle of 5° was subsequently applied to reduce the surface damage of the samples. A 200-kV aberration-corrected scanning TEM (JEM-ARM200CF, JEOL) combined with an energy-dispersive x-ray spectrometer (EDX, JED-2300T, JEOL) and an electron energy loss spectrometer (Gatan Quantum ER965) was used to obtain annular bright field and HAADF images of the samples with detector angle ranges of 12–23 mrad and 68–280 mrad, respectively. The probe-forming angle was 23 mrad, which generated an electron probe size of $\sim$ 0.8 Å. The STEM image simulation was carried out with the microscope parameters selected to approximate the experimental conditions using the QSTEM software package[6] based on the multi-slice method. Atomic-scale EDX mapping with a probe size of $\sim$ 0.1 nm and a beam current of $\sim$ 0.8 nA was performed in the same HAADF-STEM imaging mode using a dual-type silicon drift detector with 1.2 sr as an effective solid angle. EELS line scan data across the interface were recorded with an energy range of 480–990 eV to detect the O K and Fe $L_{2,3}$ edges with an energy resolution of $\sim$ 0.7 eV. The energy dispersion and dwell time per pixel were 0.25 eV/pix and 2.0 s/pix, respectively. The energy loss of the core loss EELS data was calibrated by tracking the energy drift of the zero-loss peak that was simultaneously recorded with the core loss data.

3.3. Electron holography for large scale strain mapping

Inline electron holography experiments were performed using a 200-kV aberration-corrected TEM (JEM-ARM200CF, JEOL) equipped with a Gatan GIF Quantum imaging filter system. All images were recorded using an energy filter to remove the inelastically scattered electrons outside the energy window of $\pm$5 eV. Through-focal DF, images at defocus values ranging from -4 μm to $+4$ μm were acquired by exposing a 2048×2048 pixel fiber-optically coupled UltraScan 1000 XP (Gatan, Inc.) camera for 4 s. Dark-field TEM images of a selected region were acquired with strongly excited (001) and (010) diffraction spots. The strain gradient map was obtained using the in-plane strain map (ε_{xx}), performing first-order differentiation in the [001] and [010] directions, and then obtained through vector summation.

3.4. Density functional calculations

All calculations were performed using the Vienna *ab initio* simulation package (VASP) within the framework of periodic DFT.[49] The PBEsol functional was used as the exchange–correlation functional. An effective U of 4 eV was applied for the on-site Coulomb repulsive interaction of the 3d orbitals of Fe.[50] The electron–ionic core interaction was represented by projector-augmented wave potentials. A kinetic energy cut-off of 500 eV and Γ-centered $2 \times 2 \times 2$ k-point meshes were used for the Brillouin zone integration. The calculations converged to an energy of 10^{-6} eV/cell, and the structures were allowed to relax until the forces were less than 0.001 eV/Å. A $2 \times 2 \times 2$ supercell containing 40 atoms was used to accurately reproduce G-type anti-ferromagnetic order.

4. Conclusion and perspectives

In summary, we have uncovered that mixed phases (T-, O-, and M-like phases) combined with multiple strain states (C, S, and T states) are hierarchically structured from the nanoscale to the unit-cell level for strain accommodation in a single-crystalline BFO thin film grown on a SRO/STO substrate (subjected to -1.5% strain). The multiple strain configuration developed into an irregular pattern, resulting in the formation of a random distribution of strain nanodomains as the primary level of strain accommodation. In the C and T nanodomains, it was found that extremely distorted lattices like T-like and O-like phases were mixed with M-like phases on the unit-cell scale as a secondary level of strain relief, and the population of the new distorted phases depends on the strain state of nanodomain. An important observation was that the globally integrated strain of each nanodomain points to a single value of approximately -1.5% regardless of local strain states, which is equivalent to the fully strained state (S) of the STO substrate. This phenomenological observation suggests that effective strain relief in single-crystalline BFO films can be accomplished by the multilevel reconstruction of multiple phases and strain states rather than by single-phase-mediated relaxation. This peculiar behavior for strain accommodation might be attributed to the BFO's large tolerance to strain in the film form and the availability of many metastable phases that are close in energy, which makes it possible to choose a more energetically favored route to strain accommodation. DFT calculations for the energy landscape as a function of the misfit

strain elucidate the origin of mixed-phase-mediated behavior towards strain accommodation. This study provides a critical example that microscopically resolving hidden strain order in polymorphic thin films is essential for fully understanding their strain accommodation behavior, which is required for the efficient tuning of functionalities based on strain engineering.

Acknowledgments

Project supported by Samsung Research Fundings & Incubation Center of Samsung Electronics (Grant No. SRFC-MA1702-01). Y.-M.K acknowledges partial support from the National Research Foundation of Korea (NRF) (Grant No. 2023R1A2C2002403) funded by the Korean government in Korea. A. Borisevich acknowledges support from FaCT, an Energy Frontier Research Center funded by the U.S. Department of Energy, Office of Science, Office of Basic Energy Science, Collaboratives Research Division.

References

[1] Schlom D G, Chen L Q, Eom C B, Rabe K M, Streiffer S K and Triscone J M 2007 *Annu. Rev. Mater. Res.* **37** 589
[2] Hwang J, Feng Z, Charles N, Wang X R, Lee D, Stoerzinger K A, Muy S, Rao R R, Lee D, Jacobs R, Morgan D and Shao-Horn Y 2019 *Mater. Today* **31** 100
[3] Ederer C and Spaldin N A 2005 *Phys. Rev. Lett.* **95** 257601
[4] Catalan G, Lubk A, Vlooswiik A H G, Snoeck E, Magen C, Janssens A, Rispens G, Rijnders G, Blank D H A and Noheda B 2011 *Nat. Mater.* **10** 963
[5] Chu K, Jang B K, Sung J H, Shin Y A, Lee E S, Song K, Lee J H. Woo C S, Kim S J, Kim S J, Choi S Y, Koo T Y, Kim Y H, Oh S H, Jo M H and Yang C H 2015 *Nat. Nanotechnol.* **10** 972
[6] Jeon B C, Lee D, Lee M H, Yang S M, Chae S C, Song T K, Bu S D, Chung J S, Yoon J G and Noh T W 2013 *Adv. Mater.* **25** 5643
[7] Béa H, Dupé B, Fusil S, Mattana R, Jacquet E, Warot-Fonrose B, Wilhelm F, Rogaley A, Petit S, Cors V, Anane A, Petroff F, Bouzehouane K, Geneste G, Dkhil B, Lisenkov S, Ponomareva I, Bellaiche L, Bibes M and Barthélémy A 2009 *Phys. Rev. Lett.* **102** 217603
[8] Infante I C, Lisenkov S, Dupe B, Bibes M, Fusil S, Jacquet E, Geneste G, Petit S, Courtial A, Juraszek J, Bellaiche L, Barthelemy A and Dkhil B 2010 *Phys. Rev. Lett.* **105** 057601
[9] Sando D, Agbelele A, Daumont C, Rahmedov D, Ren W, Infante I C, Lisenkov S, Prosandeev S, Fusil S, Jacquet E, Carrétéro C, Petit S, Cazayous M, Juraszek J, Breton J M L, Bellaiche L, Dhkil B, Barthélémy A and Bibes M 2014 *Philos. Trans. R. Soc. A-Math. Phys. Eng. Sci.* **372** 20120438
[10] Ramesh R and Spaldin N A 2007 *Nat. Mater.* **6** 21
[11] Dieguez O, Gonzalez-Vazquez O E, Wojdel J C and Iniguez J 2011 *Phys. Rev. B* **83** 094106
[12] Kim Y M, Kumar A, Hatt A, Morozovska A N, Tselev A, Biegalski M D, Ivanov I, Eliseev E A, Pennycook S J, Rondinelli J M, Kalinin S V and Borisevich A Y 2013 *Adv. Mater.* **25** 2497
[13] Christen H M, Nam J H, Kim H S, Hatt A J and Spaldin N A 2011 *Phys. Rev. B* **83** 144107
[14] Zeches R J, Rossell M D, Zhang J X, Hatt A J, He Q, Yang C H, Kumar A, Wang C H, Melville A, Adamo C, Sheng G, Chu Y H, Ihlefeld J F, Erni R, Ederer C, Gopalan V, Chen L Q, Schlom D G, Spaldin N A, Martin L W and Ramesh R 2009 *Science* **326** 977
[15] Chen Z, Luo A, Huang C, Yang Y Q P, You L, Hu C, Wu T, Wang J, Gao C, Sritharan T and Chen L 2011 *Adv. Funct. Mater.* **21** 133
[16] Rossell M D, Erni R, Prange M P, Idrobo J C, Luo W, Zeches R J, Pantelides S T and Ramesh R 2012 *Phys. Rev. Lett.* **108** 047601
[17] Yang Y, Schlepütz C M, Adamo C, Schlom D G and Clarke R 2013 *APL Materials* **1** 052102
[18] Saito K, Ulyanenkov A, Grossmann V, Ress H, Bruegemann L, Ohta H, Kurosawa T, Ueki S and Funakubo H 2006 *Jpn. J. Appl. Phys.* **45** 7311
[19] Kim D H, Lee H N, Biegalski M D and Christen H M 2008 *Appl. Phys. Lett.* **92** 012911
[20] Chu Y H, Zhao T, Cruz M P, Zhan Q, Yang P L, Martin L W, Huijben M, Yang C H, Zavaliche F, Zheng H and Ramesh R 2007 *Appl. Phys. Lett.* **90** 252906
[21] Lee H J, Lee S S, Kwak J H, Kim Y M, Jeong H Y, Borisevich A Y, Lee S Y, Noh D Y, Kwon O, Kim Y and Jo J Y 2016 *Scientific Reports* **6** 38724
[22] Fischer A, Kühne H and Richter H 1994 *Phys. Rev. Lett.* **73** 2712
[23] Kogan S M 1964 *Sov. Phys. Solid State* **5** 2069
[24] Lee D and Noh Tae W 2012 *Philos. Trans. R. Soc. A-Math. Phys. Eng. Sci.* **370** 4944
[25] Sando D, Barthelemy A and Bibes M 2014 *J. Phys.-Condens. Matter* **26** 473201
[26] Holcomb M B, Martin L W, Scholl A, He Q, Yu P, Yang C H, Yang S Y, Glans P A, Valvidares M, Huijben M, Kortright J B, Guo J, Chu Y H and Ramesh R 2010 *Phys. Rev. B* **81** 134406
[27] Lee S S, Kim YM, Lee H J, Seo O, Jeong H Y, He Q, Borisevich A Y, Kang B, Kwon O, Kang S, Kim Y, Koo T Y, Rhyee J S, Noh D Y, Cho B, Seo J H, Lee J H and Jo J Y 2018 *Adv. Funct. Mater.* **28** 1800839
[28] Infante I C, Lisenkov S, Dupé B, Bibes M, Fusil S, Jacquet E, Geneste G, Petit S, Courtial A, Juraszek J, Bellaiche L, Barthélémy A and Dkhil B 2010 *Phys. Rev. Lett.* **105** 057601
[29] Sando D, Agbelele A, Rahmedov D, Liu J, Rovillain P, Toulouse C, Infante I C, Pyatakov A P, Fusil S, Jacquet E, Carretero C, Deranlot C, Lisenkov S, Wang D, Le Breton J M, Cazayous M, Sacuto A, Juraszek J, Zvezdin A K, Bellaiche L, Dkhil B, Barthelemy A and Bibes M 2013 *Nat. Mater.* **12** 641
[30] Sando D, Xu B, Bellaiche L and Nagarajan V 2016 *Appl. Phys. Rev.* **3** 011106
[31] Huang C W, Chu Y H, Chen Z H, Wang J, Sritharan T, He Q, Ramesh R and Chen L 2010 *Appl. Phys. Lett.* **97** 152901
[32] Rana D S, Takahashi K, Mavani K R, Kawayama I, Murakami H, Tonouchi M, Yanagida T, Tanaka H and Kawai T 2007 *Phys. Rev. B* **75** 060405
[33] Catalan G, Sinnamon L J and Gregg J M 2004 *J. Phys.-Condes. Matter* **16** 2253
[34] Catalan G, Noheda B, McAnney J, Sinnamon L J and Gregg J M 2005 *Phys. Rev. B* **72** 020102
[35] Lee D, Yoon A, Jang S Y, Yoon J G, Chung J S, Kim M, Scott J F and Noh T W 2011 *Phys. Rev. Lett.* **107** 057602
[36] Kim Y M, He J, Biegalski M D, Ambaye H, Lauter V, Christen H M, Pantelides S T, Pennycook S J, Kalinin S V and Borisevich A Y 2012 *Nat. Mater.* **11** 888
[37] Kim Y M, Morozovska A, Eliseev E, Oxley M P, Mishra R, Selbach S M, Grande T, Pantelides S T, Kalinin S V and Borisevich A Y 2014 *Nat. Mater.* **13** 1019
[38] Hatt A J, Spaldin N A and Ederer C 2010 *Phys. Rev. B* **81** 054109
[39] Hÿtch M J, Putaux JL and Pe´nisson JM 2003 *Nature* **423** 270
[40] Tang Y L, Zhu Y L, Liu Y, Wang Y J and Ma X L 2017 *Nat. Commun.* **8** 15994
[41] Kim Y M, Lee S B, Lee J and Oh S H 2019 *Nanoscale* **11** 8281
[42] Lee J K, Park B, Song K, Jung W Y, Tyutyunnikov D, Yang T, Koch C T, Park C G, van Aken P A, Kim YM, Kim J K, Bang J, Chen L Q and Oh S H 2018 *Acta. Mater.* **145** 109
[43] Zhang N and Asle Zaeem M 2019 *npj Comput. Mater.* **5** 54
[44] Lines M E and Glass A M 2001 *Principles and Applications of Ferroelectrics and Related Materials* (Oxford: Oxford University Press)
[45] Daumont C J M, Farokhipoor S, Ferri A, WojdełJ C, Íñiguez J, Kooi B J and Noheda B 2010 *Phys. Rev. B* **81** 144115
[46] Chen Z H, Prosandeev S, Luo Z L, Ren W, Qi Y J, Huang C W, You L, Gao C, Kornev I A, Wu T, Wang J L, Yang P, Sritharan T, Bellaiche L and Chen L 2011 *Phys. Rev. B* **84** 094116
[47] Borisevich A Y, Eliseev E A, Morozovska A N, Cheng C J, Lin J Y, Chu Y H, Kan D, Takeuchi I, Nagarajan V and Kalinin S V 2012 *Nat. Commun.* **3** 775
[48] Koch C T 2002 *Determination of core structure periodicity and point defect density along dislocation* (Ph. D. Dissertation) (Arizona: Arizona State University) (in USA)
[49] Kresse G and Furthmüller J 1993 *Phys. Rev. B* **54** 11169
[50] Dudarev S L, Botton G A, Savrasov S Y, Humphreys C J and Sutton A P 1998 *Phys. Rev. B* **57** 1505